

ARTICLE

Received 9 Sep 2014 | Accepted 9 Feb 2015 | Published 12 Mar 2015

DOI: 10.1038/ncomms7577

Visualization of nanocrystal breathing modes at extreme strains

Erzsi Szilagy^{1,2,*}, Joshua S. Wittenberg^{2,*}, Timothy A. Miller³, Katie Lutker⁴, Florian Quirin⁵, Henrik Lemke⁶, Diling Zhu⁶, Matthieu Chollet⁶, Joseph Robinson⁶, Haidan Wen⁷, Klaus Sokolowski-Tinten⁵ & Aaron M. Lindenberg^{2,3,8}

Nanoscale dimensions in materials lead to unique electronic and structural properties with applications ranging from site-specific drug delivery to anodes for lithium-ion batteries. These functional properties often involve large-amplitude strains and structural modifications, and thus require an understanding of the dynamics of these processes. Here we use femtosecond X-ray scattering techniques to visualize, in real time and with atomic-scale resolution, light-induced anisotropic strains in nanocrystal spheres and rods. Strains at the percent level are observed in CdS and CdSe samples, associated with a rapid expansion followed by contraction along the nanosphere or nanorod radial direction driven by a transient carrier-induced stress. These morphological changes occur simultaneously with the first steps in the melting transition on hundreds of femtosecond timescales. This work represents the first direct real-time probe of the dynamics of these large-amplitude strains and shape changes in few-nanometre-scale particles.

¹Department of Chemistry, Stanford University, Stanford, California 94305, USA. ²Stanford Institute for Materials and Energy Sciences, SLAC National Accelerator Laboratory, 2575 Sand Hill Road, Menlo Park, California 94025, USA. ³Department of Materials Science and Engineering, Stanford University, Stanford, California 94305, USA. ⁴Department of Chemistry, University of California, Berkeley, Berkeley, California 94720, USA. ⁵Faculty of Physics and Center for Nanointegration Duisburg-Essen (CENIDE), University of Duisburg-Essen, Lotharstrasse 1, 47048 Duisburg, Germany. ⁶Linac Coherent Light Source, SLAC National Accelerator Laboratory, Menlo Park, California 94025, USA. ⁷Advanced Photon Source, Argonne National Laboratory, Argonne, Illinois 60439, USA. ⁸Stanford PULSE Institute, SLAC National Accelerator Laboratory, Menlo Park, California 94025, USA. * These authors contributed equally to this work. Correspondence and requests for materials should be addressed to A.M.L. (email: aaronl@stanford.edu).

Although extensive investigations have been carried out probing modifications in the electronic, thermodynamic and kinetic properties of semiconductor quantum dots as a function of size and shape, the size-dependent structural dynamics exhibited by nanocrystals are not well understood. For example, surface energies play a crucial role in nanoparticle phase stability, leading to size-dependent modifications of solid–liquid^{1,2} or solid–solid^{3,4} transition temperatures, but the dynamics of these transformations have not been resolved using techniques providing both atomic-scale and femtosecond resolution, the relevant length and timescales for these processes. The elastic properties and stress and strain response exhibited by nanocrystals are size dependent with novel mechanical properties emerging at the nanoscale, associated with variations in bulk moduli and the ability to withstand extreme stresses without inelastic or plastic responses^{5–9}. These properties have been utilized in the development of nanowire electrochemical cells in which ion-induced transformations are markedly modified compared with the bulk¹⁰ and in the engineering of nanoscale thin films or two-dimensional materials with unique strain-induced structural phases^{11,12}. In turn, these mechanical properties and associated anisotropic response or shape changes are intrinsically linked to the functionality and stability of nanoscale optoelectronic and nanoelectromechanical devices. As such, a real-time probe sensitive to atomic length-scale rearrangements and nanoscale morphological changes is required to elucidate their dynamical and functional response *in-situ*^{13–15}.

Time-resolved approaches utilizing optical probes have been applied previously to elucidate the elastic and acoustic response exhibited by nanomaterials. Optical pump-probe studies indirectly reflect structural responses and show evidence for breathing and extensional mode excitations, with typical periods of order 1 ps associated with sound–velocity-limited strains at the nanoscale ($1\text{ nm}/(1,000\text{ m s}^{-1}) \sim 1\text{ ps}$; refs 16–19). X-rays have been used to map the acoustic response of few hundred nanometre particles on hundreds of picosecond timescales^{20–22}. Here we use femtosecond X-ray scattering techniques to visualize the anisotropic shape changes and deformations in the limit of large strains and on femtosecond timescales. Measurement of multiple nanocrystal diffraction peaks enables the photoinduced time-dependent strains to be projected along the relevant axes of the nanostructure, independent of its orientation. For both nano-sized spheres and rods, we show that intense above-bandgap photoexcitation leads to percent level radial expansions occurring on few hundred femtosecond timescales. These are followed by a reversible contraction, with the nanocrystals exhibiting a quasi-half-cycle acoustic response. For the case of an anisotropic nanorod, we show that the expansion is anisotropic as well, with the expansion occurring only along the radial direction of the nanorod at short times, as reflected directly in the variation in the time-dependent amplitudes for different diffraction peaks. Quantitative modelling of the observed strain response for both spheres and nanorods shows that the first steps in the structural response are driven by electronic stresses rather than thermal ones, under conditions of order 1,000 electron–hole pairs/nanocrystal. Simultaneously, in this work, we resolve the structural dynamics associated with the first steps in the semiconductor nanocrystal melting process, which occur concurrently with the ultrafast strain response.

Results

Experimental setup. Figure 1 shows a schematic of the experimental setup: 70 fs full-width at half-maximum 9.5 keV ($\lambda = 1.3\text{ \AA}$) X-ray pulses generated at the Linac Coherent Light

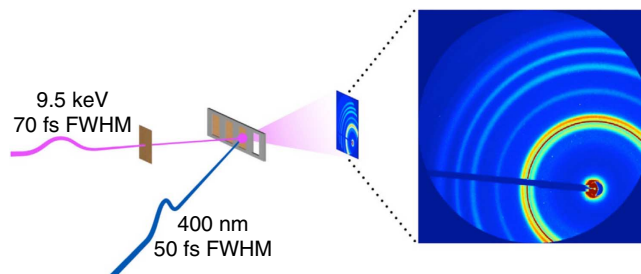


Figure 1 | Schematic of the experimental setup. Femtosecond X-ray pulse passes through X-ray timing monitor and then diffracts from $\sim 100\text{-nm}$ -thick nanocrystal powder on a Si_3N_4 membrane in a transmission geometry following above-bandgap femtosecond laser excitation. Snapshots of the time-resolved diffraction pattern are recorded on a large-area detector read out on a shot-by-shot basis. At right is raw diffraction image from CdS nanorods. FWHM, full-width at half-maximum.

Source²³ pass through a timing monitor to record the relative arrival time between pump and probe²⁴, before diffracting from a photoexcited 100-nm-thick layer of nanocrystals deposited with random orientation on a thin SiN membrane in transmission geometry (see Methods section). Also shown in Fig. 1 are raw diffraction patterns from CdS nanorods as recorded on an area detector. Figure 2 shows sample X-ray diffraction patterns for both 3.4 nm diameter CdSe spheres and $4.5 \times 18\text{ nm}$ CdS rods recorded before and 500 fs after excitation by above-bandgap 400 nm wavelength optical pulses with a laser fluence of 0.4 J cm^{-2} (Supplementary Note 1). The first seven allowed peaks of the hexagonal wurtzite structure are collected for both morphologies, with the sharp (002) reflection for the rod samples indicating that the long axis of the nanorod corresponds to the c axis of the hexagonal unit cell²⁵. The orientations for all measured lattice planes/reflections are shown as well in Fig. 2. For both the spherical and rod samples, changes in the diffraction intensity, associated with disordering processes, are superimposed on homogeneous shifts of the diffraction peaks to lower Q ($= 4\pi \sin\theta/\lambda$, where 2θ is the scattering angle shown in Fig. 2c).

Sphere and rod response. Focusing first on the case of the nanosphere response, Fig. 3 shows the time dependence of the normalized angular peak shifts $\Delta Q/Q(t)$ for all measured reflections in a few picosecond time window. All reflections are observed to have the same normalized shift within experimental error. This independence on the crystallographic direction within the sphere implies a radially symmetric strain as would be expected for an acoustic radial breathing mode. The magnitude of the peak shift indicates a maximum photoinduced strain of $\sim 1.2\%$ ($\Delta d/d = -\Delta Q/Q$ where d is a lattice spacing) corresponding to strain rates of $\sim 2 \times 10^{10}\text{ s}^{-1}$. The period of the acoustic breathing mode excitation in a spherical nanocrystal is $T = 2\pi R/(\chi c_L)$ in a continuum approximation, where R is the nanocrystal radius, χ is the first solution of the equation $\tan \chi = \chi/(1 - c_L^2/c_T^2)$, and c_L and c_T are the longitudinal and transverse wave velocities, respectively²⁶. Using known values for bulk CdSe²⁷, this gives a period of $\sim 1.1\text{ ps}$ in qualitative agreement with the observed response. This simple model does not account for the effects of the surrounding matrix but is in reasonable agreement with prior measurements¹⁷. The inset to Fig. 3a shows the long-time response ($t = 60\text{ ps}$) showing no long-lived strain induced within the signal to noise of the measurement. The observed effects for the nanospheres are therefore indicative of an isotropic radial breathing mode associated with an expansion and then contraction to the initial diameter, corresponding to one-half of an acoustic cycle.

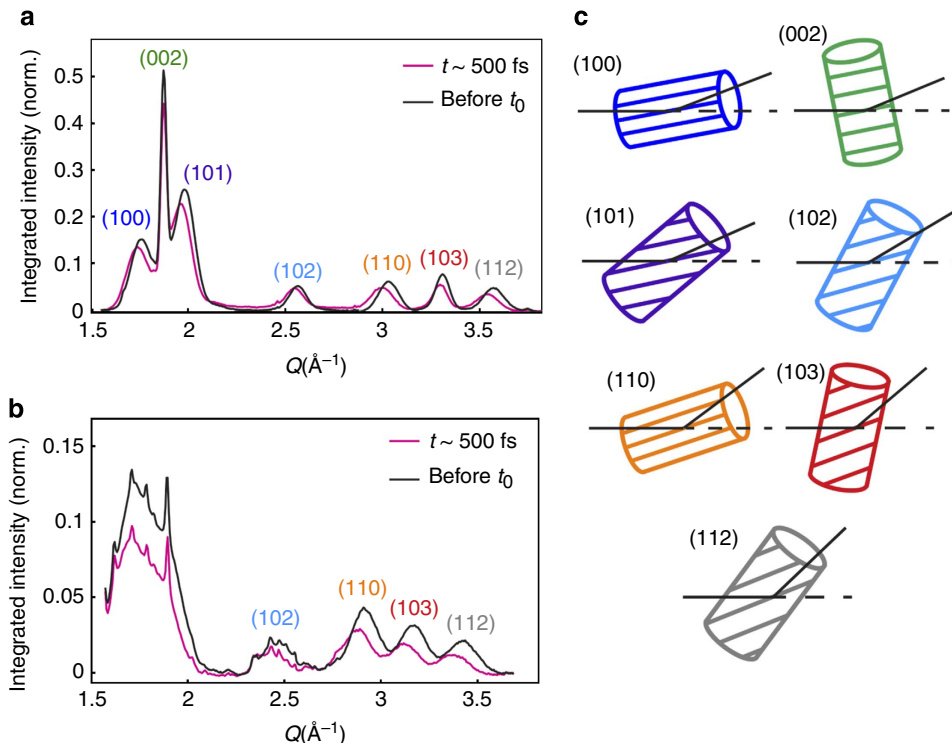


Figure 2 | Nanocrystal X-ray scattering data. (a) Azimuthally integrated Q-dependent scattering pattern from 18 × 4.5 nm CdS nanorods shown at t = 0 (black) and t = 500 fs (magenta). Miller indices are indicated for all reflections. (b) As above for CdSe 3.4 nm diameter spheres. Narrow peaks associated with organic surfactants are superimposed on the merged-together low Q reflections. (c) The orientation of each set of lattice planes probed shown with respect to the nanorod c axis, and the orientation of the nanocrystal with respect to the incident and outgoing X-ray wave vectors. Norm., normalized.

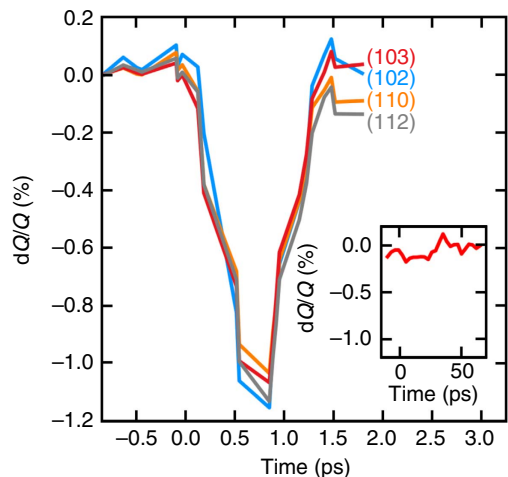


Figure 3 | Sphere radial breathing response. dQ/Q for 3.4 nm CdSe spheres for reflections indicated, showing isotropic breathing mode response with dynamics independent of the reflection probed (inset): long-time response showing no long-lived-induced strain.

In contrast to the case of the spheres where $\Delta Q/Q$ is independent of the particular X-ray reflection, the nanorod response shows a complex dependence on (hkl) (Fig. 4a), with smallest effects observed for the (002) reflection, corresponding to planes orthogonal to the long axis and no obvious dependence on Q_{hkl} . This is indicative of an anisotropic response in which changes in the interlayer lattice spacing are dependent on their orientation with respect to the nanocrystal axes. By recording peak shifts for each reflection, we are able to reconstruct the

anisotropic shape changes within the nanorod by effectively projecting the time-dependent strains along different axes of the nanostructure. We show in the following that the observed short-time response is fully consistent with a pure radial expansion of the nanowire, as observed for the case of the spheres above.

During a radial expansion, different sets of lattice planes experience different acoustic strains. For example, the (002) planes, lying perpendicular to the long axis of the nanorod, have no component along the radial direction and will experience no change in d-spacing. In contrast, the (100) and (110) planes, which are perpendicular to the radial direction, sense the radial breathing mode fully, as observed. In order to understand the response of the other reflections, consider the strain experienced by lattice planes with arbitrary angle ψ_{hkl} with respect to the (002) planes (Supplementary Fig. 1). This effect has been considered before with respect to scattering from asymmetric reflections in solids under strains normal to the surface and for uniaxial shocks and can be accounted for by including a factor of $\sin^2\psi_{\text{hkl}}$ in the relation between the strain and the fractional change in Q ^{15,28,29} (Supplementary Note 2 and Supplementary Table 1). Thus, the influence of a radial strain on the lattice spacing associated with reflection (hkl) can be written:

$$\frac{\Delta d_{\text{hkl}}}{d_{\text{hkl}}} = - \frac{\Delta Q_{\text{hkl}}}{Q_{\text{hkl}}} = \epsilon \sin^2\psi_{\text{hkl}} = \epsilon \left[1 - \frac{l^2 d_{\text{hkl}}^2}{c^2} \right] \quad (1)$$

where ϵ is the radial strain, d_{hkl} is the lattice spacing for reflection (hkl), c is the hexagonal c axis lattice constant and the right-most result is specific for the case of a hexagonal unit cell. This has the correct dependence as seen by the limiting cases for $\psi_{002} = 0$ and $\psi_{100} = \psi_{110} = \pi/2$. More generally, scaling the data after time zero for each (hkl) by the factor $\sin^2\psi_{\text{hkl}}$ collapses the complex response shown in Fig. 4a onto a single curve directly showing the

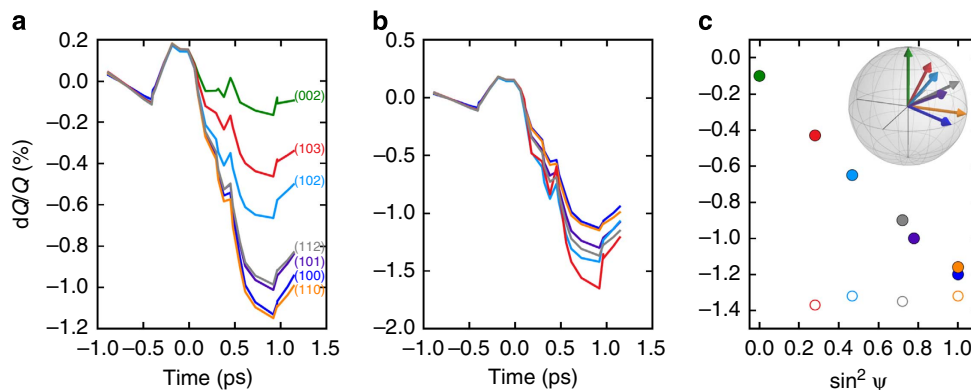


Figure 4 | Nanorod anisotropic response. (a) Nanorod time-dependent shift dQ/Q for reflections indicated showing anisotropic response. (b) Data in a scaled by factor $\sin^2\psi_{hkl}$ where ψ_{hkl} is the angle between the lattice planes with indices (hkl) and the long axis of the nanorod. (c) dQ/Q for sphere (open circles) and rod (closed circles) samples as a function of $\sin^2\psi_{hkl}$. Colours match the labelled colours at left. Inset shows different tomographic views with the long axis of the nanorod (in green) along the c axis.

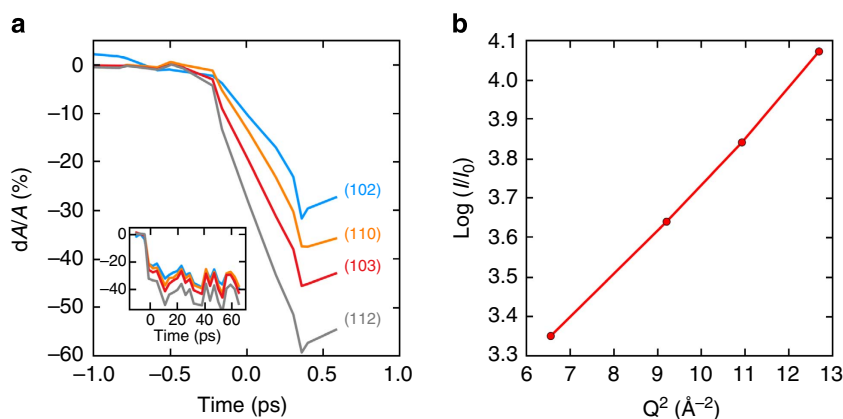


Figure 5 | Sphere disordering/melting dynamics. (a) Short timescale change in integrated area for the indicated reflections. (Inset) Long-time response showing long-lived reductions in diffracted intensity. (b) Debye-Waller fit showing logarithm of normalized scattered intensity versus Q^2 at $t = 400$ fs.

time-resolved nanowire radial strain (Fig. 4b). Alternatively, plotting the peak magnitude (at $t \sim 800$ fs) of $\Delta Q/Q_{hkl}$ as a function of $\sin^2\psi_{hkl}$ shows the expected linear dependence with slope equal to the magnitude of the radial strain, $\sim 1.2\%$ (Fig. 4b), consistent with a radial expansion as observed for the spherical geometry as shown in Fig. 4c. Together, these results show that the dynamical response of the nanowire is anisotropic, with the dominant strain associated with a radial expansion of the nanowire with no long-lived strain observed (Supplementary Fig. 2), as in the case of the spheres. Some small variation in the curves shown in Fig. 4b indicates that this model does not capture all aspects of the dynamical shape changes, but it clearly does capture the most relevant aspects. The observed timescales for this expansion are in agreement with expected values (see Methods section). At short times, this anisotropic response is as expected: extensional modes will turn on on timescales of order 10 ps but these compete with the simultaneous disordering processes discussed below.

Discussion

We observe that concurrently with the strain responses discussed above, the photoexcitation conditions used in this experiment are sufficient to drive ultrafast disordering processes within the nanocrystals, as reflected in changes in the peak intensity or integrated area of the diffraction peaks. These additional

structural responses provide a means, moreover, to understand the surprising strongly damped acoustic response shown above. Figure 5 shows time scans of the normalized integrated area dA/A for the four highest Q reflections of the 3.4-nm spheres. The timescales for the disordering process are comparable to the observed strain-induced expansion dynamics and consistent with similarly fast disordering timescales observed in bulk semiconductors^{30–33} not previously measured for the case of semiconductor nanocrystals. In contrast with the breathing mode response, the changes in integrated area persist out to the longest times probed (8 ns) (Fig. 5 inset and Supplementary Figs 3 and 4). In addition, the Q dependence of the disordering/melting response is significantly simpler than for the strain/breathing response, showing larger amplitude effects for larger Q for both spheres and rods as would be expected according to a Debye-Waller-like model, for example, $I(Q,t) = I_0 \exp(-Q^2\sigma(t)^2/3)$, where $\sigma(t)$ is the time-dependent root mean square displacement (r.m.s.d.) of the atoms³⁰. A plot of the dependence of $\log(I(t))$ on Q^2 at $t = 400$ fs (Fig. 5b) demonstrates the data's consistency with this model showing a linear dependence. We extract from the slope of this plot an r.m.s.d. of ~ 0.6 Å, comparable to the maximum radial strain-induced change in the sphere diameter and a large fraction of an interatomic spacing³⁴. Similar behaviour is observed for the rod samples (Supplementary Figs 3 and 4). Given this information, the half-cycle acoustic response observed for the nanosphere

radial breathing mode can likely be attributed to ultrafast phonon-scattering processes. These scattering processes impact the population and coherence of the induced elastic standing wave within each nanocrystal, with the scattering rates strongly increasing as a result of the extreme disorder both at the surface and within the nanocrystal. Estimates based on prior theoretical models³⁵ suggest that at temperatures of $\sim 1,000$ K (comparable to those induced within each nanocrystal—Supplementary Note 1, and Supplementary Figs 5 and 6), these scattering rates are of order 1 THz (with scattering mean free paths comparable to the nanocrystal diameter), which is consistent with the strongly damped coherent response observed. Similar acoustic damping effects in strongly photoexcited semiconductor thin films have been observed by X-ray techniques³⁶ and by optical pump-probe techniques¹⁷. The observed damping is inconsistent with dephasing associated with the finite size distribution of the nanocrystals (Supplementary Note 3). Because long-lived strain responses are not observed within the signal to noise of the measurement (for both spheres and rods; Fig. 3 inset and Supplementary Fig. 2), the applied stress must be transient, which implies a direct carrier-induced rather than temperature-driven trigger for both the disordering process and the initial breathing mode response^{37,38}. This is consistent with previous studies in bulk semiconductors that indicate a large-amplitude carrier-induced stress at short times under femtosecond excitation conditions, with the electronic stress dominating over the thermal stress³⁹. For temperature jumps of $\sim 1,000$ K, the peak strain using bulk values for the thermal expansion coefficient²⁷ is $\sim 3 \times$ smaller than the peak strain measured here and likely not resolvable within the signal to noise of the measurement (Supplementary Note 1).

Using this model, one may quantitatively fit the observed acoustic response shown in Fig. 3 to a forced simple harmonic oscillator model with damping, following previously proposed models for coherent excitation of acoustic modes in nanocrystals^{18,40}. Here the nanocrystal displacement follows the equation:

$$\ddot{x} + \frac{2\dot{x}}{\tau_D} + \omega^2 x = \sigma(t) \quad (2)$$

with x a measure of the radial strains/displacements, σ proportional to a time-dependent stress turning on at time zero and τ_D an effective damping time. Figure 6 shows best fit for the time-dependent stress and the corresponding time-dependent displacement calculated from this equation shown in comparison with the measured data for the 3.4-nm CdSe acoustic response. Good agreement is obtained for decay times and damping times of ~ 500 fs. Here the damping reflects both scattering from the induced disorder as well as coupling of the nanocrystal to the surrounding matrix. A 500-fs decay time for the applied stress is in agreement with prior studies of the ultrafast relaxation of photoexcited carriers in CdSe nanocrystals of this size: electron-hole-hole Auger processes lead to sub-picosecond timescale coupling to the lattice typically through hole relaxation without phonon bottleneck effects^{38,41,42}.

In conclusion, this work represents the first measurements of the femtosecond structural dynamics exhibited by nanocrystals in the limit of extreme strains, directly resolving the ultrafast anisotropic strain and disordering dynamics, and their coupling. New opportunities for all-optical tuning of the dynamic functionality of nanoscale devices may emerge as a result of this work. The analysis presented additionally allows for the *in situ* characterization of atomic length-scale dynamics along different crystallite directions in nanostructures with anisotropic morphologies, regardless of their orientation in space.

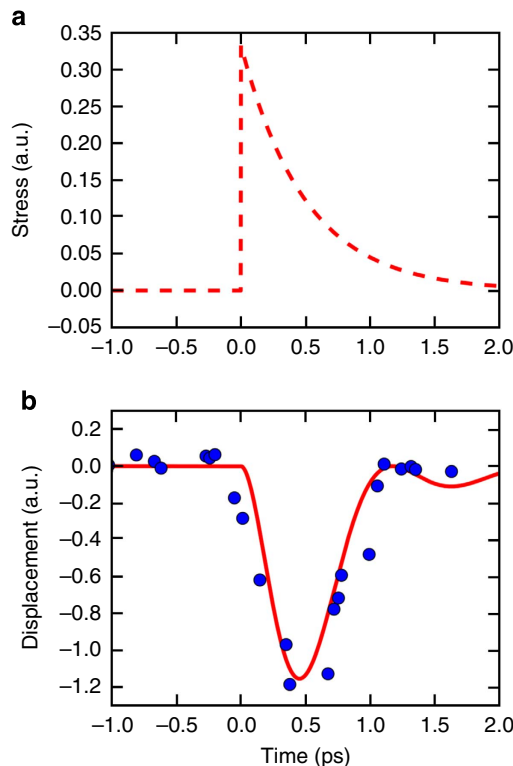


Figure 6 | Nanocrystal time-dependent stress. (a) Estimated time-dependent stress associated with acoustic breathing mode. (b) Calculated radial displacements (solid line) compared with measured data (points).

Methods

Experimental. Experiments were carried out at the Linac Coherent Light Source X-ray pump-probe hutch using hard X-ray scattering in a collinear transmission geometry at the undulator fundamental at 9.5 keV X-ray energy²³ (Fig. 1). X-ray pulses with 70 fs full-width at half-maximum pulse duration were used with the diffraction patterns recorded on a large-area MAR detector. Fifty-femtosecond optical pulses with a central wavelength of 400 nm were used to photoexcite (above bandgap) a thin ~ 100 nm layer of CdSe or CdS nanocrystals in spherical or rod morphology spin coated onto an array of Si_3N_4 membranes with random orientation as evidenced by the azimuthal symmetry of the diffraction patterns (Fig. 1). Samples were synthesized according to literature procedures²⁵ and precharacterization was carried out by transmission electron microscopy (TEM) (Supplementary Figs 7–9). Spectral encoding of the relative delay between the optical pump pulse and free electron laser (FEL) probe pulse enabled ~ 100 fs resolution of the measured nanocrystal dynamics²⁴. Single-shot X-ray diffraction patterns were collected of the nanocrystal dynamical response, and the target array was translated subsequent to each shot in order to study a fresh nanocrystal sample at all times. For each relative time delay, measurements of the static unpumped diffraction pattern were made before laser excitation using 100 X-ray shots at 1% of the peak intensity to account for sample inhomogeneity without damaging the samples before each measurement. For extraction of time-resolved changes in diffracted intensity, additional normalization of the diffraction patterns to variations in the X-ray shot-to-shot intensity was carried out using the low Q scattering from each sample position. The diffractograms were azimuthally integrated and fit to extract integrated intensity and peak position. No significant azimuthal dependence to the observed dynamics was observed. Calibration of the diffraction patterns was carried out using a LaB_6 reference sample placed in the same plane as the nanocrystal samples. For quantitative extraction of peak shifts and changes in peak area, the azimuthally integrated Q -dependent diffraction pattern was fit to the sum of Gaussians with adjustable width and position in Q space.

Breathing mode formula for a nanowire. Under photoexcitation of a nanorod of radius r , the short timescale strain response is expected to be dominated by radial expansion dynamics because of the longer required time for strains to develop along the long axis of the rod. At low excitation fluences, the expected response, following previous studies, consists of radial breathing modes with frequencies

$$\omega_{br}^{(n)} = \frac{\tau_n}{r} \sqrt{\frac{E(1-\nu)}{\rho(1+\nu)(1-2\nu)}} \quad (3)$$

where τ_n satisfies the eigenvalue equation

$$\tau_n J_0(\tau_n) = \frac{1-2\nu}{1-\nu} J_1(\tau_n) \quad (4)$$

and where E is Young's modulus, ρ is the density and ν is Poisson's ratio^{43,44}. Using tabulated values²⁷, we calculate a period of ~ 1.6 ps for a 4.5-nm CdS nanowire. Similar values are obtained for the case of the spherical geometry.

Diffraction analysis. Supplementary Note 2 derives the key relation of this paper, encoding the relationship between the observed angular shift of a nanocrystal reflection (hkl) and the angle ψ between this set of lattice planes and the planes normal to the c axis growth direction. For the case of a hexagonal unit cell, the angle between two sets of planes indexed by Miller indices (h_1, k_1, l_1) and (h_2, k_2, l_2) is given by⁴⁵:

$$\cos \Psi = \frac{h_1 h_2 + k_1 k_2 + \frac{1}{3}(h_1 k_2 + h_2 k_1) + \frac{3a^2}{4c^2} l_1 l_2}{\sqrt{(h_1^2 + k_1^2 + h_1 k_1 + \frac{3a^2}{4c^2} l_1^2)(h_2^2 + k_2^2 + h_2 k_2 + \frac{3a^2}{4c^2} l_2^2)}} \quad (5)$$

This relation is used to calculate the relevant angles between the vectors [hkl] and [002]. Supplementary Table 1 gives the calculated values for all reflections used in this paper.

References

- Goldstein, A., Echer, C. & Alivisatos, A. Melting in semiconductor nanocrystals. *Science* **256**, 1425–1427 (1992).
- Buffat, P. & Borel, J. P. Size effect on the melting temperature of gold particles. *Phys. Rev. A* **13**, 2287 (1976).
- Zheng, H. *et al.* Observation of transient structural-transformation dynamics in a Cu₂S nanorod. *Science* **333**, 206–209 (2011).
- Zhang, H., Gilbert, B., Huang, F. & Banfield, J. F. Water-driven structure transformation in nanoparticles at room temperature. *Nature* **424**, 1025–1029 (2003).
- Chen, C., Shi, Y., Zhang, Y., Zhu, J. & Yan, Y. Size dependence of Young's modulus in ZnO nanowires. *Phys. Rev. Lett.* **96**, 075505 (2006).
- Yu, D., Feng, J. & Hone, J. Elastically strained nanowires and atomic sheets. *MRS Bull.* **39**, 157–162 (2014).
- Li, J., Shan, Z. & Ma, E. Elastic strain engineering for unprecedented materials properties. *MRS Bull.* **39**, 108–114 (2014).
- Zhu, T. & Li, J. Ultra-strength materials. *Prog. Mater. Sci.* **55**, 710–757 (2010).
- Juvé, V. *et al.* Probing elasticity at the nanoscale: terahertz acoustic vibration of small metal nanoparticles. *Nano Lett.* **10**, 1853–1858 (2010).
- Chan, C. K. *et al.* High-performance lithium battery anodes using silicon nanowires. *Nat. Nanotechnol.* **3**, 31–35 (2007).
- Schlom, D. G. *et al.* Elastic strain engineering of ferroic oxides. *MRS Bull.* **39**, 118–130 (2014).
- Duerloo, K. N., Li, Y. & Reed, E. J. Structural phase transitions in two-dimensional Mo- and W-dichalcogenide monolayers. *Nat. Commun.* **5**, 4214 (2014).
- Miller, T. A. *et al.* The mechanism of ultrafast structural switching in superionic copper (I) sulphide nanocrystals. *Nat. Commun.* **4**, 1369 (2013).
- Daranciang, D. *et al.* Ultrafast photovoltaic response in ferroelectric nanolayers. *Phys. Rev. Lett.* **108**, 087601 (2012).
- Wittenberg, J. S. *et al.* Real-time visualization of nanocrystal solid–solid transformation pathways. *Nano Lett.* **14**, 1995–1999 (2014).
- Cerullo, G., De Silvestri, S. & Banin, U. Size-dependent dynamics of coherent acoustic phonons in nanocrystal quantum dots. *Phys. Rev. B* **60**, 1928 (1999).
- Son, D. H., Wittenberg, J. S., Banin, U. & Alivisatos, A. P. Second harmonic generation and confined acoustic phonons in highly excited semiconductor nanocrystals. *J. Phys. Chem. B* **110**, 19884–19890 (2011).
- Hartland, G. V. Coherent excitation of vibrational modes in metallic nanoparticles. *Annu. Rev. Phys. Chem.* **57**, 403–430 (2006).
- Hodak, J. H., Henglein, A. & Hartland, G. V. Size dependent properties of Au particles: coherent excitation and dephasing of acoustic vibrational modes. *J. Chem. Phys.* **111**, 8613 (1999).
- Mariager, S. O. *et al.* Direct observation of acoustic oscillations in InAs nanowires. *Nano Lett.* **10**, 2461–2465 (2010).
- Clark, J. N. *et al.* Ultrafast three-dimensional imaging of lattice dynamics in individual gold nanocrystals. *Science* **341**, 56–59 (2013).
- Plech, A., Kotaidis, V., Gresillon, S., Dahmen, C. & Plessen, G. V. Laser-induced heating and melting of gold nanoparticles studied by time-resolved x-ray scattering. *Phys. Rev. B* **70**, 195423 (2004).
- Emma, P. *et al.* First lasing and operation of an angstrom-wavelength free-electron laser. *Nat. Photon.* **4**, 641 (2010).
- Harmand, M. *et al.* Achieving few-femtosecond time-sorting at hard X-ray free-electron lasers. *Nat. Photon.* **7**, 215 (2013).
- Peng, X. *et al.* Shape control of CdSe nanocrystals. *Nature* **404**, 59–61 (2000).
- Lamb, H. On the vibrations of an elastic sphere. *Proc. London Math. Soc.* **s1-13**, 189–212 (1881).
- Adachi, S. *Handbook on Physical Properties of Semiconductors* 273–309 (Springer, 2004).
- Lings, B., Wark, J. S., DeCamp, M. F., Reis, D. A. & Fahy, S. Simulations of time-resolved x-ray diffraction in Laue geometry. *J. Phys. Condens. Matter* **18**, 9231–9244 (2006).
- Milathianaki, D. *et al.* Femtosecond visualization of lattice dynamics in shock-compressed matter. *Science* **342**, 220–223 (2013).
- Lindenberg, A. M. *et al.* Atomic-scale visualization of inertial dynamics. *Science* **308**, 392–395 (2005).
- Sciaini, G. *et al.* Electronic acceleration of atomic motions and disordering in bismuth. *Nature* **457**, 56–59 (2009).
- Sokolowski-Tinten, K. *et al.* Femtosecond x-ray measurement of ultrafast melting and large acoustic transients. *Phys. Rev. Lett.* **87**, 225701 (2001).
- Lindenberg, A. M. *et al.* X-ray diffuse scattering measurements of nucleation dynamics at femtosecond resolution. *Phys. Rev. Lett.* **100**, 135502 (2008).
- Lindemann, F. A. The calculation of molecular vibration frequencies. *Physik. Z.* **11**, 609 (1910).
- Tamura, S. & Maris, H. J. Temperature-dependence of phonon lifetimes in dielectric crystals. *Phys. Rev. B* **51**, 2857–2863 (1995).
- Cavalleri, A. *et al.* Anharmonic lattice dynamics in germanium measured with ultrafast x-ray diffraction. *Phys. Rev. Lett.* **85**, 586–589 (2000).
- Hannah, D. C. *et al.* Direct measurement of lattice dynamics and optical phonon excitation in semiconductor nanocrystals using femtosecond stimulated Raman spectroscopy. *Phys. Rev. Lett.* **111**, 107401 (2013).
- Klimov, V., McBranch, D., Leatherdale, C. & Bawendi, M. Electron and hole relaxation pathways in semiconductor quantum dots. *Phys. Rev. B* **60**, 13740 (1999).
- Nie, S., Wang, X., Park, H., Clinite, R. & Cao, J. Measurement of the electronic Grüneisen constant using femtosecond electron diffraction. *Phys. Rev. Lett.* **96**, 025901 (2006).
- Perner, M. *et al.* Observation of hot-electron pressure in the vibration dynamics of metal nanoparticles. *Phys. Rev. Lett.* **85**, 792–795 (2000).
- Pietryga, J., Zhuravlev, K., Whitehead, M., Klimov, V. & Schaller, R. Evidence for barrierless Auger recombination in PbSe nanocrystals: a pressure-dependent study of transient optical absorption. *Phys. Rev. Lett.* **101**, 217401 (2008).
- Kilina, S. V., Kilin, D. S. & Prezhdo, O. V. Breaking the phonon bottleneck in PbSe and CdSe quantum dots: time-domain density functional theory of charge carrier relaxation. *ACS Nano* **3**, 93–99 (2009).
- Hu, M. *et al.* Vibrational response of nanorods to ultrafast laser induced heating: theoretical and experimental analysis. *J. Am. Chem. Soc.* **125**, 14925–14933 (2003).
- Lange, H., Mohr, M., Artemyev, M., Woggon, U. & Thomsen, C. Direct observation of the radial breathing mode in CdSe nanorods. *Nano Lett.* **8**, 4614–4617 (2008).
- Kelly, A. A. & Knowles, K. M. *Crystallography and Crystal defects* (John Wiley & Sons, 2012).

Acknowledgements

This work was supported by the Department of Energy, Basic Energy Sciences, Materials Sciences and Engineering Division. Portions of this research were carried out at the Linac Coherent Light Source (LCLS) at the SLAC National Accelerator Laboratory. LCLS is an Office of Science User Facility operated for the US Department of Energy (DOE) Office of Science by Stanford University. H.W. acknowledges support from the U.S. DOE, Office of Science, under contract no. DE-AC02-06CH11357. F.Q. and K.S.-T. gratefully acknowledge financial support by the German Research Council through the Collaborative Research Center SFB 616 'Energy Dissipation at Surfaces'. K.L. was supported by the Physical Chemistry of Inorganic Nanostructures Program, KC3105, Director, Office of Science, Office of Basic Energy Sciences of the US DOE under contract no. DE-AC02-05CH11231.

Author contributions

J.S.W., E.S., T.A.M., K.L., F.Q., H.L., D.Z., M.C., J.R., H.W., K.S.-T. and A.M.L. carried out the experiment. K.L., J.S.W. and E.S. made the samples. A.M.L. initiated the project and conceived the work. E.S., J.S.W. and A.M.L. wrote the manuscript with input from all authors.

Additional information

Supplementary Information accompanies this paper at <http://www.nature.com/naturecommunications>

Competing financial interests: The authors declare no competing financial interests.

Reprints and permission information is available online at <http://npg.nature.com/reprintsandpermissions/>

How to cite this article: Szilagy, E. *et al.* Visualization of nanocrystal breathing modes at extreme strains. *Nat. Commun.* 6:6577 doi: 10.1038/ncomms7577 (2015).